

First-principles calculations on strain tunable hyperfine Stark shift of shallow donors in Si

Zi-Kai Zhou(周子凯) and Jun Kang(康俊)

Multiple anomalous Hall effect in kagome metal TbV_5MnSn_6

Zi-Cheng Tao(陶咨成), Yi-Xuan Luo(罗伊轩), Shi-Hao Zhang(张世豪), and Yan-Feng Guo(郭艳峰)

Citation: Chin. Phys. B, 2025, 34 (**8**): 087103. DOI: 10.1088/1674-1056/add5cc
http://cpb.iphy.ac.cn; http://iopscience.iop.org/cpb

What follows is a list of articles you may be interested in

Visualizing the electronic structure of kagome magnet $LuMn_6Sn_6$ by angle-resolved photoemission spectroscopy

Man Li(李满), Qi Wang(王琦), Liqin Zhou(周丽琴), Wenhua Song(宋文华), Huan Ma(马欢), Pengfei Ding(丁鹏飞), Alexander Fedorov, Yaobo Huang(黄耀波), Bernd Büchner, Hechang Lei(雷和畅), Shancai Wang(王善才), and Rui Lou(娄睿)

Chin. Phys. B, 2024, 33 (**11**): 117101. DOI: 10.1088/1674-1056/ad7afe

Two-dimensional Sb net generated nontrivial topological states in $SmAgSb_2$ probed by quantum oscillations

Jian Yuan(袁健), Xian-Biao Shi(石贤彪), Hong Du(杜红), Tian Li(李田), Chuan-Ying Xi(郗传英), Xia Wang(王霞), Wei Xia(夏威), Bao-Tian Wang(王保田), Rui-Dan Zhong(钟瑞丹), and Yan-Feng Guo(郭艳峰)

Chin. Phys. B, 2024, 33 (**7**): 077102. DOI: 10.1088/1674-1056/ad4bc2

Spin direction dependent quantum anomalous Hall effect in two-dimensional ferromagnetic materials

Yu-Xian Yang(杨宇贤) and Chang-Wen Zhang(张昌文)

Chin. Phys. B, 2024, 33 (**4**): 047101. DOI: 10.1088/1674-1056/ad1380

Design of sign-reversible Berry phase effect in 2D magneto-valley material

Yue-Tong Han(韩曰通), Yu-Xian Yang(杨宇贤), Ping Li(李萍), and Chang-Wen Zhang(张昌文)

Chin. Phys. B, 2023, 32 (**9**): 097101. DOI: 10.1088/1674-1056/acd920

Exchange couplings in magnetic films

Liu Wei (刘伟), Liu Xiong-Hua (刘雄华), Cui Wei-Bin (崔伟斌), Gong Wen-Jie (龚文杰), Zhang Zhi-Dong (张志东)

Chin. Phys. B, 2013, 22 (**2**): 027104. DOI: 10.1088/1674-1056/22/2/027104

RAPID COMMUNICATION

Multiple anomalous Hall effect in kagome metal TbV_5MnSn_6

Zi-Cheng Tao(陶咨成)[1,†], Yi-Xuan Luo(罗伊轩)[1,†], Shi-Hao Zhang(张世豪)[2,‡], and Yan-Feng Guo(郭艳峰)[1,3,§]

[1] *State Key Laboratory of Quantum Functional Materials, School of Physical Science and Technology, ShanghaiTech University, Shanghai* 201210, *China*
[2] *School of Physics and Electronics, Hunan University, Changsha* 410082, *China*
[3] *ShanghaiTech Laboratory for Topological Physics, ShanghaiTech University, Shanghai* 201210, *China*

(Received 24 March 2025; revised manuscript received 26 April 2025; accepted manuscript online 8 May 2025)

The kagome lattice hosts unique electronic structure with Dirac fermions, van Hove singularities, and flat bands, which has been subjected to intensive study in recent years. We report herein the observation of significantly enhanced magnetism including a very large coercive magnetic field up to 4.7 T, optimized magnetic energy product with the maximum value of 45 kJ/m^3, and an increased magnetic ordering temperature reaching 113 K in Mn-substituted kagome metal TbV_6Sn_6, namely, TbV_5MnSn_6. Besides, both topological Hall-like and anomalous Hall effects are detected, with the latter being primarily dominated by intrinsic Berry curvature as indicated by our data analysis and theoretical calculations. Our work establishes an effective route for engineering the physical properties of kagome magnets. The results also provide valuable insights into the interplay between magnetism and topological states of the kagome lattice.

Keywords: kagome magnet, magnetotransport, Hall effect

PACS: 71.20.Be, 75.47.–m, 75.50.Cc

DOI: 10.1088/1674-1056/add5cc **CSTR:** 32038.14.CPB.add5cc

1. Introduction

The kagome lattice, a geometrically frustrated structure composed of corner-sharing triangular motifs, naturally hosts Dirac fermions, flat bands and van Hove singularities in its electronic structure.[1–6] Besides the vast attention that has been paid to these intriguing characteristics, considerable research interest has also been arrested in the correlation between the magnetism and the peculiar electronic structure of kagome magnets.[7,8] Further experimental investigations have revealed that the rare-earth-based kagome magnets *R*166 (RX_6Y_6, R = rare earth, X = Cr, Mn, Fe, Co, and Y = Sn, Ge) exhibit a rich diversity of magnetic ground states.[9–19] In particular, the Mn/Fe-based kagome lattices demonstrate long-range magnetic order even persisting above the room temperature, which initially motivated extensive exploration for practical applications. Recently, this family of materials has drawn vast attention as an ideal platform for investigating emergent quantum phenomena, such as tunable Chern quantum phase, flat band, exchange bias effect, and topological Hall effect.[20–24]

The discovery of superconductivity and charge-density-wave order in V-based kagome metals AV_3Sb_5 (A = K, Rb, Cs) has stimulated intense research on V-based kagome lattice, particularly the RV_6Sn_6 compounds isostructural with the *R*166 family.[25–37] In these V-based kagome systems, the V-based kagome sublattice remains nonmagnetic while localized moments originate from magnetic rare-earth elements on the *R*-site.[38–40] Robust kagome electronic features, including Dirac cones and flat bands, have been experimentally confirmed across this series.[41–44] In particular, TbV_6Sn_6 manifests Ising ferromagnetism with uniaxial anisotropy below $T_C = 4.3$ K, accompanied by anomalous Hall effect (AHE) suggestive of Chern gap formation analogous to that in $TbMn_6Sn_6$.[45,46] However, recent spectroscopic evidence challenges the conventional time-reversal-symmetry-breaking mechanism for Dirac gap opening in TbV_6Sn_6, instead proposing strong spin–orbit coupling (SOC) as the origin, which leads to a non-zero spin Berry curvature.[47]

In this work, we report on the single crystal growth of TbV_6Sn_6 with partial substitution of the V kagome lattice by Mn atoms as TbV_5MnSn_6. Combining magnetization measurements, magnetotransport characterizations, and density functional theory (DFT) calculations, we systematically investigated the physical properties induced by Mn substitution effects on TbV_6Sn_6. Our measurements unveiled intriguing behaviors including topological Hall-like (THE-like) effect and intrinsic AHE, which are correlated with its distinctive magnetic properties, such as exceptionally large coercive field ($\mu_0 H_c \approx 4.7$ T) and enhanced magnetic energy product (45 kJ/m^3). These results demonstrate the feasibility of manipulating electronic structure topology in kagome metals through chemical substitution.

[†] These authors contributed equally to this work.
[‡] Corresponding author. E-mail: zhangshh@hnu.edu.cn
[§] Corresponding author. E-mail: guoyf@shanghaitech.edu.cn

© 2025 Chinese Physical Society and IOP Publishing Ltd. All rights, including for text and data mining, AI training, and similar technologies, are reserved.

2. Experimental details

Single crystals of TbV_5MnSn_6 were grown by using the flux method. Starting materials of Tb pieces (99.9%, Macklin), Mn pieces (99.9%, Macklin), V powder (99.9%, Macklin) and Sn grains (99.99%, Macklin) were mixed in a molar ratio of 1:1:5:20 and placed into an alumina crucible, which were then sealed into a quartz tube in vacuum. The assembly was heated in a furnace up to 1050 °C within 10 h, kept at the temperature for 10 h, and then slowly cooled down to 700 °C at a temperature decreasing rate of 2 °C/h. The excess flux was removed at this temperature by quickly placing the assembly into a high-speed centrifuge. Hexagonal crystals with the size of 2 mm were left in the alumina crucible.

The compositions were examined on a Phenom Pro scanning electron microscope with the energy dispersive x-ray spectroscopy (EDS). The analysis shows that Tb:V:Mn:Sn = 1.17:4.91:1:6.62, which is close to the nominal 1:5:1:6, demonstrating the stoichiometry of the crystals. The single-crystal x-ray diffraction (SXRD) data were collected on a Bruker D8 single-crystal x-ray diffractometer with Mo $K_{\alpha 1}$ ($\lambda = 0.71073$ Å) at 278 K. The powder XRD (PXRD) was carried out on a Bruker D8 Advance powder x-ray diffractometer with Cu $K_{\alpha 1}$ ($\lambda = 1.54184$ Å) at 298 K. The collected SXRD and PXRD data were analyzed by using the Olex2 and GSAS-II softwares, respectively.[48,49]

The electrical and magnetotransport measurements, including the resistivity and Hall effect measurements, were carried out by using a standard Hall bar geometry in a commercial DynaCool physical properties measurement system from Quantum Design. The magnetic susceptibility measurements were performed on a Quantum Design magnetic properties measurement system.

We carried out first-principles calculations within the framework of the generalized gradient approximation functional of the density functional theory through employing the Vienna *ab initio* simulation package (VASP) with projector augmented wave method.[50–52] To simplify the calculations, single-site occupation for Mn atoms was assumed. In all calculations, we employed the Hubbard parameter $U = 7$ eV on the f-orbitals of Tb atoms. We projected Bloch states to Wannier functions, and then used the WannierTools package to calculate the intrinsic anomalous Hall conductivity with $301 \times 301 \times 181$ k-point mesh.[53–55]

3. Results

The crystal structure of TbV_5MnSn_6 is drawn based on the PXRD data refinement, which is featured by the stacked $\cdots$–$TbSn_2$–$(V/Mn)_3$–Sn–Sn_2–Sn–$(V/Mn)_3$–$TbSn_2$–$\cdots$ layers along the c-axis and the ideal kagome layer formed by the V/Mn layer, as illustrated in Fig. 1(a). The diffraction patterns could be well indexed on the basis of a hexagonal unit cell with the space group *P6/mmm* (No. 191) with the lattice parameters $a = b = 5.53$ Å, $c = 9.17$ Å, and $\alpha = \beta = 90°$, $\gamma = 120°$. The SXRD analysis demonstrates that all atom positions at *mm*2 (0.5, 0.5, 0.754) are occupied by V atoms, and the preferred site of the substituted Mn atoms cannot be distinguished. This conclusion is supported by the exceptionally low reliability factors ($R = 1.72\%$ and $wR_2 = 3.87\%$), indicating high reliability of the refinement results. Thus, Mn atoms exhibit random distribution patterns at the V site. The refinement results were summarized in Table S1 of the supplementary information (SI). The occupancy of each atom derived from the PXRD refinement is given in Table 1, also showing that all Mn atoms are situated at *mm*2 (0.5, 0.5, 0.754) and their occupancy is 0.16, which is close to 1/6. The SXRD data presented in Figs. 1(c)–1(e) demonstrate the phase purity and high crystal quality of TbV_5MnSn_6, indicating by the perfect reciprocal space lattice without any other miscellaneous points.

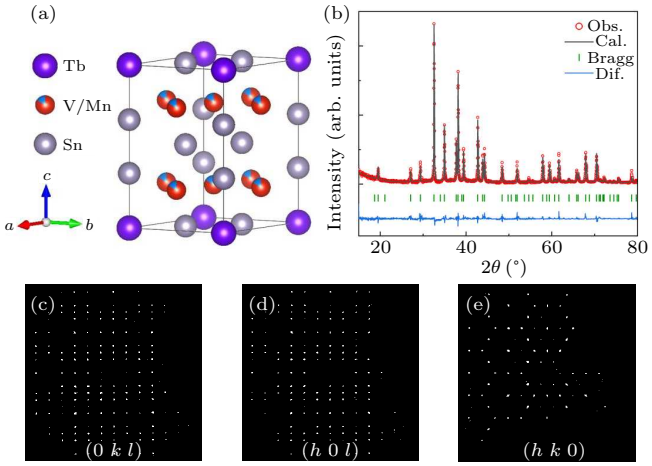


Fig. 1. (a) Schematic view of the TbV_5MnSn_6 crystal structure. (b) Powder XRD diffraction patterns of TbV_5MnSn_6. (c)–(e) The diffraction patterns in the reciprocal space along (0kl), (h0l), and (hk0) directions.

Table 1. The refined parameters from PXRD measurements.

Site	Wyckoff	Symmetry	x	y	z	Occupation	Uiso
Tb1	1*b*	6/*mmm*	0	0	0	1	0.00855
Sn1	2*d*	–6*m*2	2/3	1/3	0	1	0.00069
Sn2	2*e*	6*mm*	0	0	0.664	1	0.00533
Sn3	2*c*	–6*m*2	2/3	1/3	1/2	1	0.01091
Mn1	6*i*	*mm*2	1/2	1/2	0.754	0.16	0.03578
V1	6*i*	*mm*2	1/2	1/2	0.754	0.84	0.00020

The temperature dependent magnetization of TbV_5MnSn_6 at $\mu_0 H = 0.1$ T is presented in Fig. 2(a), exhibiting multiple magnetic transitions with increasing temperature. The magnetic phase diagram can be classified into three distinct regions: (i) the FM ground state with parallel alignment of both Tb and Mn spins below $T_2 = 42$ K, (ii) the ferrimagnetic (FIM) state displaying parallel-aligned Mn moments coupled with antiparallel-aligned Tb moments, as illustrated in Fig. 2(b), and (iii) the paramagnetic state above $T_1 = 113$ K. The random distribution of Mn atoms in TbV_5MnSn_6 results

in magnetic clusters in which Tb moments adopt antiparallel alignment with neighboring Mn moments. These magnetic clusters exhibit two characteristic temperature dependencies. One is that the reduced thermal energy allows gradual cluster growth and slower moment reorientation, accounting for the FIM characteristics observed in the isothermal magnetization curves between 110 K and 40 K, as demonstrated in Figs. 2(b) and 3(d). This behavior is similar to that of other rare earth-transition metal systems with unequal magnetic sublattices.[56–58] Another one is below 40 K, the clusters are connected and therefore require a higher external field to switch the whole Tb sublattice, which gives rise to a large hysteresis loop, while the loop disappears above 40 K. Besides, the slope of field-cooling magnetization $\mathrm{d}M/\mathrm{d}T$ also displays two turning points, as indicated by the arrows in Fig. S1 of the SI. The magnetizations at 2 K remain stable prior to field reversal, subsequently displaying two-step variations corresponding to direction reversal of Mn and Tb magnetic moments, respectively. In contrast, the curve at 45 K shows absence of hysteresis loop and stepwise features, indicating the existence of the FIM state. It is worth noting that the magnetization curves above 110 K exhibit linear behavior, suggesting essentially a paramagnetic state. It should be noted that the current results do not completely preclude contributions from spin dynamics.[59] More efforts to uncover the underlying physics are very necessary. The inset of Fig. 2(a) displays the fitting results by using the Curie–Weiss law $\chi(T) = C/(T-\theta_C)$, which yield an effective magnetic moment $\mu_{\mathrm{eff}} = 11.36\mu_B$ and a Weiss temperature $\theta_C = -92$ K, consistent with the high-temperature FIM behavior. At 2 K, TbV_5MnSn_6 demonstrates remarkable magnetic characteristics with the saturation magnetization $\mu_{\mathrm{sat}} = 10.7\mu_B$, the zero-field magnetization $\mu_{\mathrm{rem}} = 10.2\mu_B$, and the coercive field $B_c(\mu_0 H_c) = 4.7$ T. The calculated maximum magnetic energy product $(B/H)_{\mathrm{max}}$ at 2 K is 45 kJ/m^3, as shown in Fig. 2(c). This value significantly exceeds the performance capabilities of conventional ferrites and alnicos.[60] Table 2 provides a detailed comparison of TbV_5MnSn_6 and commercial permanent magnets about their characteristic parameters in the performance metrics and application potential.

Table 2. Characteristics parameters for typical commercial-oriented magnets, TbV_6Sn_6, $TbMn_6Sn_6$, and TbV_5MnSn_6.

	B_r (T)	J_S (T)	iH_c (kA/m)	B_c (T)	$(B/H)_{\mathrm{max}}$ (kJ/m^3)
$SrFe_{12}O_{19}$	0.41	0.47	275	0.33	34
Alnico	1.25	1.40	54	0.07	43
TbV_6Sn_6	0.04	0.45	18	0.04	0.2
$TbMn_6Sn_6$	0.19	0.20	15	3.7	7.2
TbV_5MnSn_6 (this work)	0.49	0.51	374	4.7	45
$SmCo_5$	0.88	0.95	1700	0.83	150
Sm_2Co_{17}	1.08	1.15	800	1.01	220
$Nd_2Fe_{14}B$	1.28	1.54	1000	1.13	300

B_r: remanence; J_S: saturation polarization; iH_c: intrinsic coercivity; $B_c(\mu_0 H_c)$: coercivity; $(B/H)_{\mathrm{max}}$: maximum magnetic energy product. The data is collected from Refs. [46,60,61].

The rare-earth permanent magnets have revolutionized modern magnetic engineering as a cornerstone material system, distinguished by exceptional magnetic characteristics including high remanent magnetization, pronounced intrinsic magnetic anisotropy, and superior demagnetization resistance.[60] The paradigmatic Mn-based kagome magnet $TbMn_6Sn_6$ exemplifies this conundrum, but its strong interlayer Tb–Mn AFM coupling necessitates ultrahigh magnetic fields (> 100 T) for full spin polarization, thus critically limiting practical implementation.[62,63] As a contrast, TbV_6Sn_6, with a nonmagnetic V-based kagome lattice, reveals compromised performance through suppressed magnetic ordering temperatures (4.1 K) resulting from weakened Tb–Tb exchange interactions, coupled with low coercive fields (B_c < 0.5 T).[46] Our results implement a crystal engineering strategy to achieve desired magnetic properties through Mn substitution in the V-based kagome lattice. The above unveiled significantly improved magnetic hardness at low temperatures with a remarkably enhanced coercivity of $B_c = 4.7$ T and maximum energy product $(B/H)_{\mathrm{max}}$ of about 45 kJ/m^3, thus establishing a novel research pathway of kagome magnets for use as permanent magnets.

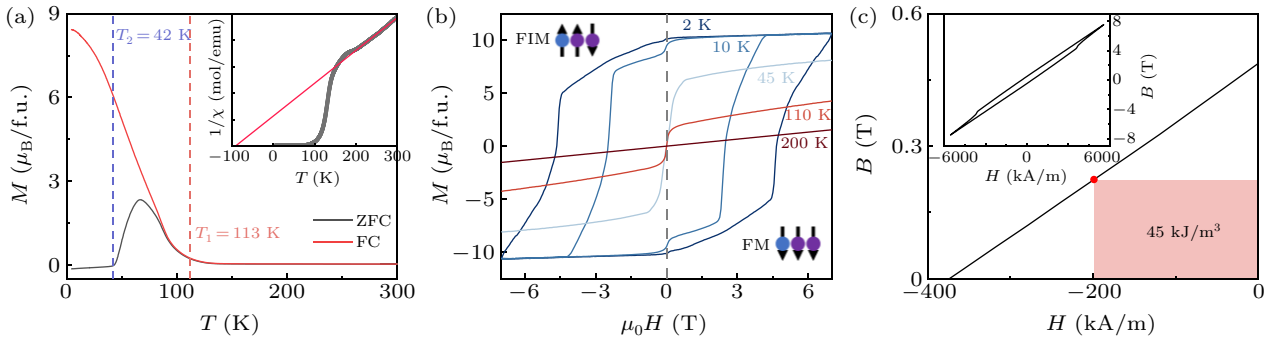


Fig. 2. (a) Temperature dependence of magnetizations along the c-axis at $\mu H = 0.1$ T. Inset displays the fitting results of Curie–Weiss law. (b) The field dependence of magnetizations M for H along the c-axis at various temperatures of 2 K, 10 K, 45 K, 110 K, and 200 K. Arrows denote the orientations of Mn (blue) and Tb (purple) moments. (c) The maximum magnetic energy product at 2 K. Inset shows full diagram of magnetic energy product at 2 K.

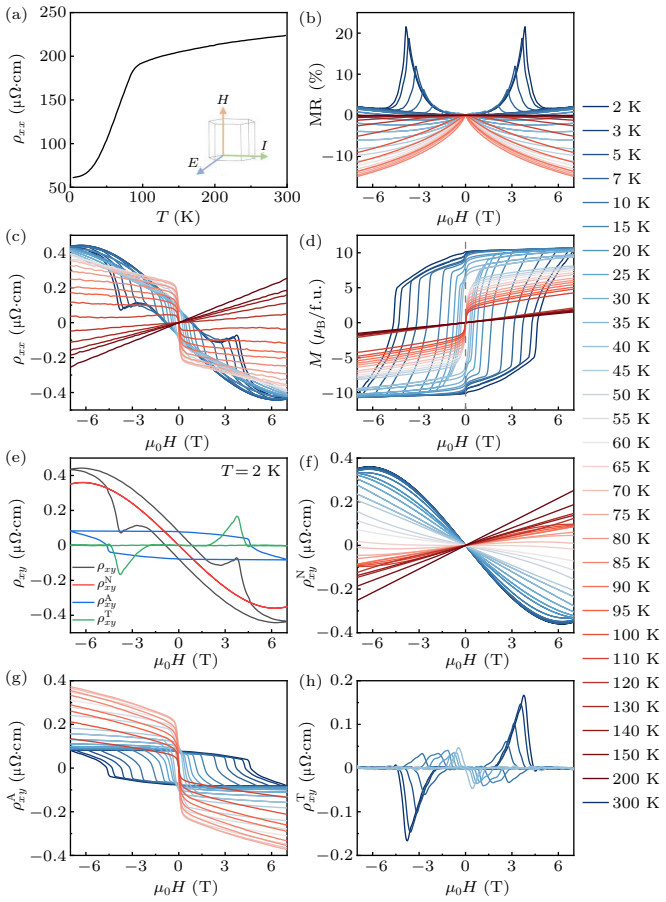


Fig. 3. (a) Temperature dependent longitudinal resistivity ρ_{xx}. The inset shows the measurement configuration for ρ_{xy} of TbV_5MnSn_6. The field dependence of (a) magnetoresistance, (b) transverse resistivity ρ_{xy}, and (c) magnetizations M at various temperatures for H along the c-axis. (e) The extracted ordinary (ρ_{xy}^{N}), anomalous (ρ_{xy}^{A}), and THE-like (ρ_{xy}^{T}) Hall resistivities from the total Hall resistivity (ρ_{xy}) at 2 K. The different components of Hall resistivity for (f) ordinary Hall resistivity ρ_{xy}^{N}, (g) anomalous Hall resistivity ρ_{xy}^{A}, and (h) THE-like Hall resistivity ρ_{xy}^{T} extracted from Eq. (1), at various temperatures for H along the c-axis.

To elucidate the effects of Mn substitution on the magnetizations, electrical and magnetotransport properties of TbV_5MnSn_6, the temperature dependent longitudinal resistivity $\rho_{xx}(T)$, the magnetoresistance (MR), the transverse resistivity ρ_{xy}, and the isothermal magnetizations $M(H)$ under magnetic field applied along the c-axis are shown in Figs. 3(a)–3(d), respectively. The temperature dependent longitudinal resistivity $\rho_{xx}(T)$ of TbV_5MnSn_6 is presented in Fig. 3(a), which unveils the semi-metallic nature in the temperature range of 2–300 K. As shown in Fig. 3(b), the MR, defined as $[\rho(\mu_0 H) - \rho(0)]/\rho(0) \times 100\%$ where $\rho(\mu_0 H)$ and $\rho(0)$ represent the resistivity with and without the magnetic field, respectively, remains clear hysteresis below 40 K, which is consistent with the $M(H)$ behaviors. The MR evolves from positive to negative as the temperature increases, with its magnitude gradually diminishing. This behavior might stem from the competition between classical magnetoresistance dominated by Lorentz force effects and negative MR contributions arising from spin rearrangement processes. In general, the MR curves could offer valuable insights into the spin rearrangement process and hence the evolution of magnetic structure. However, in our case, the MR magnitude remains rather small ($< \pm 0.1\%$ near the small step on the $M(H)$ curves, as shown in Fig. S2 of the SI), making it challenging to resolve potential correlations with the small step observed in the $M(H)$ curves. However, the large peak on the MR curves is clear, which corresponds to a large suppression of the scattering arising from the Tb moments switching.

4. Analysis and discussion

Now we analyze the Hall effect in TbV_5MnSn_6 which exhibits complex behaviors arising from multiple contributions. In general, ρ_{xy} can be expressed as

$$\rho_{xy} = \rho_{xy}^{N} + \rho_{xy}^{A} + \rho_{xy}^{T}, \tag{1}$$

where ρ_{xy}^{N} represents ordinary Hall resistivity, ρ_{xy}^{A} ($= R_S 4\pi M$) is anomalous Hall resistivity with R_S denoting the anomalous Hall coefficient, and ρ_{xy}^{T} represents the THE-like resistivity.[64–66] To quantitatively estimate the densities and mobilities of the carriers, ρ_{xy}^{N} was fitted by employing the conventional two-band model

$$\rho_{xy}^{N} = \frac{\left(n_h \mu_h^2 - n_e \mu_e^2\right) + \mu_h^2 \mu_e^2 \left(n_h - n_e\right) B^2}{\left(n_e \mu_e + n_h \mu_h\right)^2 + \mu_h^2 \mu_e^2 \left(n_h - n_e\right)^2 B^2} \cdot \frac{B}{e}, \tag{2}$$

where n_e (n_h) denotes the carrier density for the electrons (holes), and μ_e (μ_h) is the mobility of the electrons (holes). The fitting results of n_e (n_h) and μ_e (μ_h) at different temperatures are summarized in Fig. 4. Figure 3(e) presents the fitting results at 2 K, where total Hall resistivity is separated into three distinct components including ρ_{xy}^{N}, ρ_{xy}^{A}, and ρ_{xy}^{T}. The extracted ρ_{xy}^{N}, ρ_{xy}^{A}, and ρ_{xy}^{T} are depicted in Figs. 3(f)–3(h), respectively, indicating the multiple contributions to the Hall effects in TbV_5MnSn_6. Notably, the topological Hall-like effect vanishes abruptly at 40 K, coinciding with a characteristic transition observed in both carrier density and mobility around this critical temperature, which should be ascribed to the complex exchange interactions between Tb and incomplete kagome magnetic sublattices induced by Mn/V-mixed kagome layers.

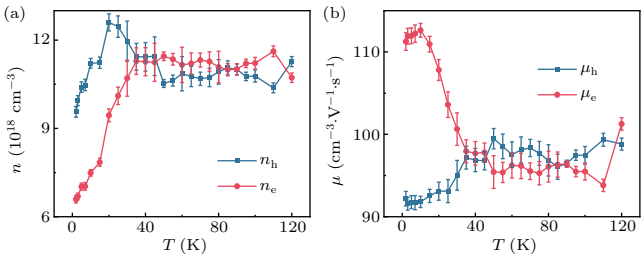


Fig. 4. (a) The holes (n_h) and electrons (n_e) carrier densities at different temperatures. (b) The holes (μ_h) and electrons (μ_e) mobilities at different temperatures.

In order to investigate the effects of partial Mn substitution for the V kagome lattice on the electronic band structure of TbV_6Sn_6, the first-principles calculations on TbV_5MnSn_6 were carried out. While magnetic measurements suggest the FM ground state for TbV_5MnSn_6, our calculations reveal the FIM configuration as the energetically favorable state. Consequently, both FM and FIM configurations were systematically considered, with corresponding magnetic structures being depicted in Figs. 5(a) and 5(b), respectively. The calculated magnetic moments yield 7.38μ_B for Tb and 2.82μ_B for Mn. The total moment is determined as 10.2μ_B per formula unit in the FM state, consistent with experimental magnetization data at 2 K. In contrast, the FIM configuration shows a reduced total moment of 4.6μ_B. The corresponding band structures are shown in Figs. 5(c) and 5(d). We note that accidental band crossings near the Fermi level along the X–Γ direction plotted within the green ring in the FIM state are all gapped in the FM state, while those along the Y–K direction plotted within the purple ring in the FM state are all gapped in the FIM state. Thus, different accidental band crossings in the FM and FIM states provide different intrinsic anomalous Hall conductivity (AHC). In the FM and FIM states, the energy bands near the Fermi level are both mainly contributed by the d-orbitals of Mn and V atoms. Previous studies indicate that Tb moments diminish with rising temperature, exerting negligible impact on the AHC.[46] However, the AHC, defined as $\sigma_{xy}^{A} = -\rho_{xy}^{A}/(\rho_{xy}^{A\,2} + \rho_{xx}^{2})$, exhibits a decrease with increasing temperature, which can be attributed to enhanced spin fluctuation of Mn with increasing temperature. Fitting to the $\log(\rho_{xy}^{A})$ against the $\log(\rho_{xx})$ curve by using the formula $\rho_{xy}^{A} \propto \rho_{xx}^{\alpha}$ yields the scaling exponents α of 2.03, thus excluding extrinsic skew-scattering ($\rho_{xy}^{A} \propto \rho_{xx}$) as the dominant mechanism, as shown in the inset of Fig. 5(e).[67] As shown in Fig. 5(f), the calculated intrinsic AHC contributed by different magnetic domains cancels each other, and produces a magnitude equal to the experiment value of 16.14 $\Omega^{-1}\cdot cm^{-1}$, indicating the contribution from the intrinsic Berry curvature.[68] However, we note that the relatively small AHC actually makes it somewhat complicated to trace other possibilities as the real sources. The calculated density of states (DOS) is presented in Fig. 5(g). While DFT calculations reveal numerous energy bands near the Fermi level, the associated DOS remains rather small, which can explain the semi-metallic characteristics in TbV_5MnSn_6, as shown in the fitting results and the resistivity presented in Fig. 3(a). Considering potential complexities of the fitting due to multiple contributions in the Hall effect, the THE-like effect extracted from Eq. (1) may incorporate contributions from ordinary Hall components, thus introducing uncertainties in carrier density estimation. However, the characteristic transitions of carrier densities and mobilities at 40 K were actually confirmed, coinciding with the disappearance of THE-like effect. Notably, the THE-like conductivity defined as $\sigma_{xy}^{T} = -\rho_{xy}^{T}/(\rho_{xy}^{T\,2} + \rho_{xx}^{2})$ clearly surpasses the AHC at low temperatures, as seen in Fig. 5(e), suggesting the significant interplay between intricate magnetic behavior and transport properties in this system.

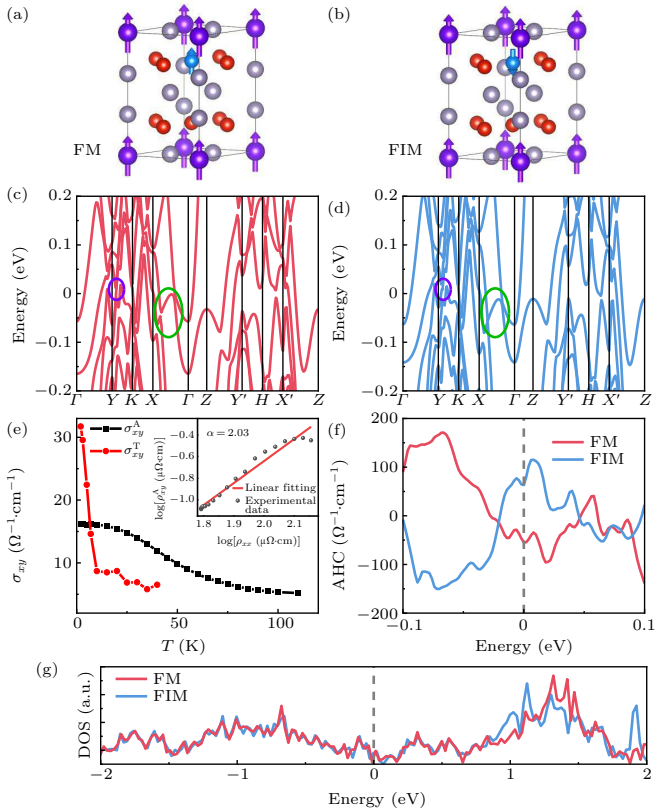


Fig. 5. (a), (b) The magnetic structures of FM state and FIM state in TbV_5MnSn_6. (c), (d) The corresponding band structures. (e) The extracted σ_{xy}^{A} and σ_{xy}^{T} at various temperatures. Inset shows the plot of $\log(\rho_{xy}^{A})$ against $\log(\rho_{xx})$. (f) The calculated σ_{xy}^{A} within the energy range of −0.1 eV to 0.1 eV around the Fermi energy. (g) Total densities of states in the vicinity of E_F.

5. Conclusion

To summarize, the partial Mn substitution for V in the kagome metal TbV_6Sn_6 results in exceptional magnetic properties, including substantial coercive fields and enhanced maximum magnetic energy products. Besides, it also leads to topological Hall-like effect and anomalous Hall effect originating from intrinsic Berry curvature, which provides an opportunity to study the intriguing magnetic structure and exotic electronic states. Our work offers an excellent platform for investigating the interplay between magnetism and electronic band structure topology in the kagome lattice. The results are also instructive for band structure engineering in kagome magnets as well as for designing functional magnetoelectric materials. Future investigations should integrate advanced characterization techniques to construct microscopic phase diagrams of magnetic structural evolution and elucidate the interplay between complex magnetic orders and nontrivial band structure topology.

Acknowledgments

Project supported by the National Key R&D Program of China (Grant Nos. 2024YFA1400066, 2023YFA1406100, and 2024YFA1410300), the open research fund of Beijing National Laboratory for Condensed Matter Physics (Grant No. 2023BNLCMPKF002), the National Natural Science Foundation of China (Grant No. 12304217), Analytical Instrumentation Center (Grant No. SPST-AIC10112914), and the Double First-Class Initiative Fund of ShanghaiTech University.

References

[1] Yin J X, Pan S H H and Hasan M Z 2021 *Nat. Rev. Phys.* **3** 249
[2] Neupert T, Denner M M, Yin J X, Thomale R and Hasan M Z 2022 *Nat. Phys.* **18** 137
[3] Jiang K, Wu T, Yin J X, Wang Z Y, Hasan M Z, Wilson S D, Chen X H and Hu J P 2023 *Natl. Sci. Rev.* **10** nwac199
[4] Yin J X, Lian B and Hasan M Z 2022 *Nature* **612** 647
[5] Xu X T, Yin J X, Qu Z and Jia S 2023 *Rep. Prog. Phys.* **86** 114502
[6] Li M, Ma H, Lou R and Wang S C 2025 *Chin. Phys. B* **34** 017101
[7] Mielke A 1991 *J. Phys. A* **24** L73
[8] Syôzi I 1951 *Prog. Theor. Phys.* **6** 306
[9] Wang Y B, Wiards D, Ryan D H and Cadogan J M 1994 *IEEE Trans. Magn.* **30** 4951
[10] Venturini G, Welter R and Malaman B 1992 *J. Alloys Compd.* **185** 99
[11] Brabers J H V J, Duijn V H M, Deboer F R and Buschow K H J 1993 *J. Alloys Compd.* **198** 127
[12] Rosenfeld E V and Mushnikov N V 2008 *Physica B* **403** 1898
[13] Cadogan J M and Ryan D H 2001 *J. Alloys Compd.* **326** 166
[14] Brabers J H V J, Buschow K H J and Deboer F R 1994 *J. Alloys Compd.* **205** 77
[15] SchobingerPapamantellos P, RodriguezCarvajal J and Buschow K H J 1997 *J. Alloys Compd.* **256** 92
[16] Yang X Y, Zeng Q Q, He M, Xu X T, Du H F and Qu Z 2024 *Chin. Phys. B* **33** 077501
[17] Fedyna M F, Skolozdra R V and Gorelenko Y K 1999 *Inorg. Mater.* **35** 373
[18] Li L F, Chi S W, Ma W L, Guo K Z, Xu G and Jia S 2024 *Chin. Phys. B* **33** 057501
[19] Lyu M, Liu Y, Zhang S, Liu J Y, Yang J Y, Wang Y B, Feng Y T, Dong X B, Wang B B, Wei H X and Liu E K 2024 *Chin. Phys. B* **33** 107507
[20] Yin J X, Ma W L, Cochran T A, *et al*. 2020 *Nature* **583** 533
[21] Ma W L, Xu X T, Yin J X, Yang H, Zhou H B, Cheng Z J, Huang Y Q, Qu Z, Wang F, Hasan M Z and Jia S 2021 *Phys. Rev. Lett.* **126** 246602
[22] Li M, Wang Q, Wang G W, Yuan Z H, Song W H, Lou R, Liu Z T, Huang Y B, Liu Z H, Lei H C, Yin Z P and Wang S C 2021 *Nat. Commun.* **12** 3129
[23] Yang T Y, Wan Q, Song J P, Du Z, Tang J, Wang Z W, Plumb N C, Radovic M, Wang G W, Wang G Y, Sun Z, Yin J X, Chen Z H, Huang Y B, Yu R, Shi M, Xiong Y M and Xu N 2022 *Quantum Front.* **1** 14
[24] Zhang H D, Koo J, Xu C Q, Sretenovic M, Yan B H and Ke X L 2022 *Nat. Commun.* **13** 1091
[25] Ortiz B R, Teicher S M L, Hu Y, Zuo J L, Sarte P M, Schueller E C, Abeykoon A M M, Krogstad M J, Rosenkranz S, Osborn R, Seshadri R, Balents L, He J F and Wilson S D 2020 *Phys. Rev. Lett.* **125** 247002
[26] Ortiz B R, Gomes L C, Morey J R, *et al.* 2019 *Phys. Rev. Mater.* **3** 094407
[27] Xu H S, Yan Y J, Yin R T, Xia W, Fang S J, Chen Z Y, Li Y J, Yang W Q, Guo Y F and Feng D L 2021 *Phys. Rev. Lett.* **127** 187004
[28] Liu Z H, Zhao N N, Yin Q W, Gong C S, Tu Z J, Li M, Song W H, Liu Z T, Shen D W, Huang Y B, Liu K, Lei H C and Wang S C 2021 *Phys. Rev. X* **11** 041010
[29] Cho S, Ma H Y, Xia W, Yang Y C, Liu Z T, Huang Z, Jiang Z C, Lu X L, Liu J S, Liu Z H, Li J, Wang J H, Liu Y, Jia J F, Guo Y F, Liu J P and Shen D W 2021 *Phys. Rev. Lett.* **127** 236401
[30] Li H X, Zhang T T, Yilmaz T, *et al.* 2021 *Phys. Rev. X* **11** 031050
[31] Tan H X, Liu Y Z, Wang Z Q and Yan B H 2021 *Phys. Rev. Lett.* **127** 046401
[32] Xiao Q, Lin Y, Li Q, Zheng X, Francoual S, Plueckthun C, Xia W, Qiu Q, Zhang S, Guo Y, Feng J and Peng Y 2023 *Phys. Rev. Research* **5** L012032
[33] Xiao Q, Li Q Z, Liu J J, Li Y K, Xia W, Zheng X Q, Guo Y F, Wang Z W and Peng Y Y 2023 *Phys. Rev. Mater.* **7** 074801
[34] Jiang Y X, Yin J X, Denner M M, *et al.* 2021 *Nat. Mater.* **20** 1353
[35] Wu Q, Wang Z X, Liu Q M, Li R S, Xu S X, Yin Q W, Gong C S, Tu Z J, Lei H C, Dong T and Wang N L 2022 *Phys. Rev. B* **106** 205109
[36] Xu Y S, Ni Z L, Liu Y Z, Ortiz B R, Deng Q W, Wilson S D, Yan B H, Balents L and Wu L 2022 *Nat. Phys.* **18** 1470
[37] Li H, Zhao H, Ortiz B R, Park T, Ye M X, Balents L, Wang Z Q, Wilson S D and Zeljkovic I 2022 *Nat. Phys.* **18** 265
[38] Lee J and Mun E 2022 *Phys. Rev. Mater.* **6** 083401
[39] Zhang X X, Liu Z Y, Cui Q, Guo Q, Wang N N, Shi L F, Zhang H, Wang W H, Dong X L, Sun J P, Dun Z and Cheng J G 2022 *Phys. Rev. Mater.* **6** 105001
[40] Zeng X Y, Wang H, Wang X Y, Lin J F, Gong J, Ma X P, Han K, Wang Y T, Dai Z Y and Xia T L 2024 *Phys. Rev. B* **109** 104412
[41] Peng S T, Han Y L, Pokharel G, Shen J C, Li Z Y, Hashimoto M, Lu D H, Ortiz B R, Luo Y, Li H C, Guo M Y, Wang B Q, Cui S T, Sun Z, Qiao Z H, Wilson S D and He J F 2021 *Phys. Rev. Lett.* **127** 266401
[42] Huang X, Cui Z Q, Huang C X, Huo M W, Liu H, Li J Y, Liang F X, Chen L, Sun H L, Shen B, Zhang Y W and Wang M 2023 *Phys. Rev. Mater.* **7** 054403
[43] Ding J Y, Zhao N N, Tao Z C, Huang Z, Jiang Z C, Yang Y C, Cho S H Y, Liu Z T, Liu J S, Guo Y F, Liu K, Liu Z H and Shen D W 2023 *J. Phys.:Condens. Mat.* **35** 405502
[44] Kong X M, Tao Z C, Zhang R, Xia W, Chen X, Pei C Y, Ying T P, Qi Y P, Guo Y F, Yang X F and Li S Y 2024 *Chin. Phys. Lett.* **41** 047503
[45] Pokharel G, Ortiz B, Chamorro J, Sarte P, Kautzsch L, Wu G, Ruff J and Wilson S D 2022 *Phys. Rev. Mater.* **6** 104202
[46] Rosenberg E, DeStefano J M, Guo Y C, Oh J S, Hashimoto M, Lu D H, Birgeneau R J, Lee Y B, Ke L Q, Yi M and Chu J H 2022 *Phys. Rev. B* **106** 115139
[47] Li H, Cheng S Y, Pokharel G, Eck P, Bigi C, Mazzola F, Sangiovanni G, Wilson S D, Di Sante D, Wang Z Q and Zeljkovic I 2024 *Nat. Phys.* **20** 1103
[48] Dolomanov O V, Bourhis L J, Gildea R J, Howard J A K and Puschmann H 2009 *J. Appl. Crystallogr.* **42** 339
[49] Toby B H and Von Dreele R B 2013 *J. Appl. Crystallogr.* **46** 544
[50] Perdew J P, Burke K and Ernzerhof M 1996 *Phys. Rev. Lett.* **77** 3865
[51] Kresse G and Hafner J 1993 *Phys. Rev. B* **47** 558
[52] Blochl P E 1994 *Phys. Rev. B* **50** 17953
[53] Mostofi A A, Yates J R, Lee Y S, Souza I, Vanderbilt D and Marzari N 2008 *Comput. Phys. Commun.* **178** 685
[54] Marzari N, Mostofi A A, Yates J R, Souza I and Vanderbilt D 2012 *Rev. Mod. Phys.* **84** 1419
[55] Wu Q S, Zhang S N, Song H F, Troyer M and Soluyanov A A 2018 *Comput. Phys. Commun.* **224** 405
[56] Huang Y Q, Zheng P Y, Liu R, Xu X T, Wu Z Y, Dong C, Wang J F, Yin Z P and Jia S 2023 *Chin. Phys. B* **32** 107502
[57] Becker J, Tsukamoto A, Kirilyuk A, Maan J C, Rasing T, Christianen P C M and Kimel A V 2017 *Phys. Rev. Lett.* **118** 117203
[58] Bhatt R C, Ye L X, Hai N T, Wu J C and Wu T H 2021 *J. Magn. Magn. Mater.* **537** 168196
[59] Mielke C, Ma W L, Pomjakushin V, *et al*. 2022 *Commun. Phys.* **5** 107
[60] Coey J M D 2002 *J. Magn. Magn. Mater.* **248** 441
[61] Riberolles S X M, Slade T J, Abernathy D L, Granroth G E, Li B, Lee Y, Canfield P C, Ueland B G, Ke L Q and McQueeney R J 2022 *Phys. Rev. X* **12** 021043
[62] Nil L, Trevisan T V and Mcqueeney R J 2025 *Phys. Rev. B* **111** 054410
[63] Xu X T, Yin J X, Ma W L, Tien H J, Qiang X B, Reddy P V S, Zhou H B, Shen J, Lu H Z, Chang T R, Qu Z and Jia S 2022 *Nat. Commun.* **13** 1197
[64] Pugh E M and Lippert T W 1932 *Phys. Rev.* **42** 709
[65] Nagaosa N, Sinova J, Onoda S, MacDonald A H and Ong N P 2010 *Rev. Mod. Phys.* **82** 1539
[66] Wang H, Dai Y Y, Chow G M and Chen J S 2022 *Prog. Mater. Sci.* **130** 100971
[67] Smit J 1958 *Physica* **24** 39
[68] Karplus R and Luttinger J M 1954 *Phys. Rev. B* **95** 1154